Journal of Mechanical Engineering and Automation 2016, 6(5): 117-127
DOI: 10.5923/j.jmea.20160605.04

Damage Assessment of a Large-Scale Hybrid Composite Wind Turbine Blade

Norimichi Nanami[1,*], Ozden O. Ochoa[2]

[1]Department of Mechanical Engineering, Nihon University, Tokyo, Japan
[2]Department of Mechanical Engineering, Texas A&M University, College Station, USA

Abstract Wind energy is realistically poised to meet the demands of an increasing world population with economic viability. The size of the horizontal-axis wind turbines (HAWT) has increased rapidly to match this higher energy demand, leading to an exponential increase in the blade weight. A credible approach to reduce weight is to utilize hybrid composites such as carbon and glass fiber (CF/GF) reinforced polymers to improve specific stiffness/strength and damage tolerance. Herein, we present our design and damage assessment study of a large-scale hybrid composite HAWT blade under static and dynamic conditions representative of aerodynamic and bird impact loads. Static analyses identified core damage and local wrinkling as primary modes, and the blade configuration provided excellent damage tolerance below wind speed of 8.72 m/s. The bird impact simulations at the blade tip revealed that the reinforcement architecture and geometry successfully survived the direct impact event without incurring any damage in the composites. The oblique impact led to local matrix tensile damage in the skin and the core damage at the impact site without any penetration.

Keywords Coupled Eulerian-Lagrangian analysis, Damage initiation and evolution, Bird strike

1. Introduction

Wind energy is one of the most promising and mature alternatives to meet the energy needs of economic growth and population increase. It is capable of providing 72 TW (TW = 10^{12} W) of electric power, which is approximately four times the world energy consumption in 2012 [1, 2]. Thus, wind energy market has grown rapidly in the last couple of decades, boosting up the size of wind turbines to generate higher power output [3]. Mostly, a horizontal-axis wind turbine (HAWT) with propeller type blades is utilized in a large-scale wind power system, and its configuration as an upwind land-based construction is schematically depicted in Figure 1. The joining concept, internal structure, and damage assessment of the 80 m wind turbine blade has been studied in detail and reported by Nanami [4-6].

In general, large-scale HAWTs have either two or three blades, with both cylindrical and airfoil cross-sections. The cylindrical section is located near the blade root, where the blade is attached to the hub by means of metallic bolts [7]. Then, the blade transitions from the cylindrical cross-section to an airfoil cross-section which determines its aerodynamic performance. Low-drag airfoils are being developed at various institutes in the US and Europe to improve the aerodynamic characteristics of airfoils specifically for wind turbines [8-10]. Typically, the blade consists of an upper and a lower blade skin, spar cap, and shear web, which are bonded together as depicted in Figure 2. The skin and web are usually of sandwich construction comprised of GF fabric and/or unidirectional GF (UD-GF) reinforced polymers for the face sheet and polymeric foams, balsa wood, or honeycomb type as the core material. For a large-scale HAWT blade, a hybrid CF/GF composite laminate was often employed in the construction of the spar cap.

Additionally, constant thickness was employed for the face sheet, and thickness of the core and spar cap laminate was defined as a function of the airfoil chord length [11-14].

In addition to aerodynamic loads during service, the blade is also exposed to various impact scenarios such as bird strike and hail storm where safe operation and subsequent safe shut down are of significant importance. As the local stiffness of the blade changes due to impact, the probability of inducing dynamic instability increases. Thus, the study of damage mechanism of the blade caused by impact is of crucial importance. Impact velocity, impact location, and bird weight for typical bird strike cases were guided by data from Dahlroth [15]. Lagrangian, Coupled Eulerian-Lagrangian (CEL), Arbitrary Lagrangian-Eulerian (ALE), and Smoothed-Particle Hydrodynamics (SPH) modeling are all suitable approaches and are widely used in bird strike simulations [16-18]. Since a bird is mostly

* Corresponding author:
nnanami@mech.cst.nihon-u.ac.jp (Norimichi Nanami)
Published online at http://journal.sapub.org/jmea

composed of water, the artificial bird is akin to hydrodynamic representation with a simple geometry such as a cylinder, an ellipsoid, or a sphere [17-20].

Herein, we computationally perform damage assessment of a large-scale hybrid composite HAWT blade under static and dynamic loading conditions in Abaqus, commercial finite element analysis (FEA) software. Aerodynamic loads and bird impact loads are considered with various airfoil and composite architecture configurations to demonstrate the feasibility and advantages of utilizing CF/GF reinforcements and to gather insight to damage mechanisms.

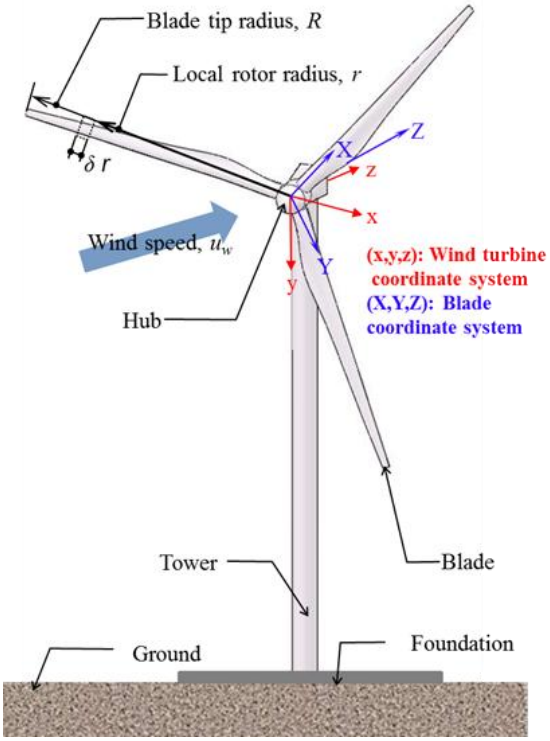

Figure 1. Schematic of a typical HAWT

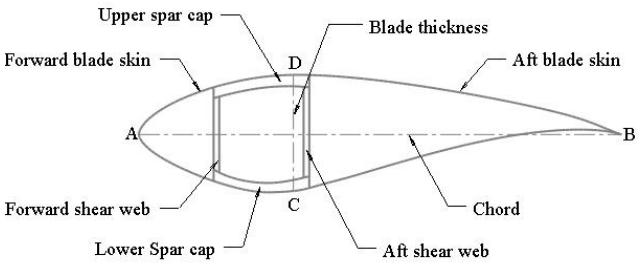

Figure 2. Schematic of cross-section of the blade

2. Blade Description

The overall geometry including airfoil construction and material selections are presented in the following sections. The blade of our 8MW wind turbine (herein referred to as SW45) has a blade tip radius of 80 m and is positioned at a 140 m hub-height [21]. The composite layers (thickness-orientation-material) solely reflect our damage tolerant design efforts with target weight reduction.

2.1. Geometry Specifics

The full blade geometry is represented in SolidWorks as shown in Figure 3. Although practical wind turbine blades are pre-twisted along the rotor radius, their pre-twist angle distribution is neglected for simplicity in the present model. The thick-airfoil family (NREL S816, S817, S818) is employed for the blade because of its excellent aerodynamic performance [8].

The blade in this study is generated based on the following non-dimensional specifications: The non-dimensional chord distribution along the rotor radius is taken from Griffin [13, 14]. The blade cross-section shape and ratio of the blade thickness to the chord length along the rotor radius are provided by Somers [8]. Spar cap and shear web as internal reinforcements of the blade are constructed in the airfoil section (5.6 m < r < 80 m). To improve buckling stability in the blade, the forward and aft shear web are attached at the recommended positions [13, 14]. Spar cap is located between the forward and aft shear web. Dorsally the spar cap width remains constant between r = 5.6 m and r = 20 m, and this width is linearly decreased further to the blade tip.

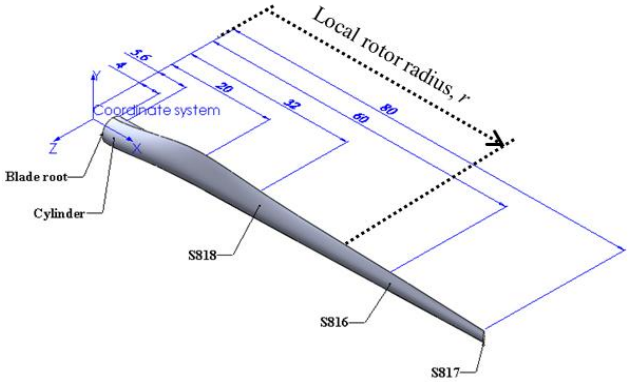

Figure 3. Dimensions of the 80 m blade

2.2. Composite Layup

The root section (4 m < r < 5.6 m) of the blade consists of GF fabric layers. Since metallic bolts with a large diameter are installed into the blade root connected to the hub, this root section usually experiences high stresses which are mitigated with the selection of 40 mm thick laminate. In the airfoil section (5.6 m < r < 80 m), sandwich constructions of GF face sheets with balsa core are employed in the forward/aft blade skin (FBS/ABS) and shear web (SW). The face sheet of the skin is GF fabric layer, and the face in the web is laminated with GF fabric and ±45 ° UD-GF layers. The spar cap (SC) laminate is composed of 15% CF fabric and 85% UD-GF layers by volume. The full composite lay-up is presented in [4]. Properties of both the skin and spar cap laminates are assigned to the skin between the forward and aft shear web as depicted in Figure 2 creating the

asymmetric section stiffness matrix.

The laminate thickness in the airfoil section is determined as a function of the airfoil chord length as summarized in Table 1. The thickness of the spar cap laminate and balsa core is assigned as a step function to incorporate a gradual taper in laminate thickness.

Table 1. Thickness Distribution in the Airfoil Section in Meters

r	Face sheet	Balsa core			SC
		FBS	ABS	SW	
5.6-20	0.002	0.032	0.054	0.054	0.074
20-32	0.002	0.036	0.060	0.060	0.036
32-46	0.002	0.030	0.050	0.050	0.029
46-60	0.001	0.020	0.044	0.032	0.022
60-70	0.001	0.016	0.035	0.025	0.016
70-75	0.001	0.013	0.029	0.021	0.012
75-80	0.001	0.011	0.025	0.018	0.009

2.3. Tip Sectional Profile

A 5m tip sectional blade (TSB5M blade) is extracted from the full SW45 blade to simulate bird impact studies. All geometries and laminate details used in the sectional blade are the same as those located between r = 75 m and r = 80 m of the SW45 blade.

3. Soft Body Impact Representation

3.1. Constitutive Model

An equation of state (EOS) material model is adopted as an approximation for the constitutive model of a bird (soft body impactor). In this linear model, pressure is obtained from Equation (1) which represents the coupling of pressure and internal energy [22]:

$$p = \frac{\rho_0 c_0^2 \eta}{(1-s\eta)^2}\left(1-\frac{\Gamma_0 \eta}{2}\right)+\Gamma_0 \rho_0 E_m \quad (1)$$

Note that $\rho_0 {c_0}^2$ is equivalent to the elastic bulk modulus at small nominal strains. The linear relationship between the shock velocity and the particle velocity is defined through s as expressed in Equation (2).

$$U_s = c_0 + sU_p \quad (2)$$

The total duration of an impact event is estimated in Equation (3) [17].

$$t_d = L/U_0 \quad (3)$$

Since the EOS model describes only the hydrostatic behavior of an impactor, a deviatoric behavior uncoupled with volumetric response can be defined to take into account shear strength of an impactor. The deviatoric stress tensor for the Newtonian viscous shear behavior is expressed in Equation (4) [22].

$$\mathbf{S} = 2\eta_v \dot{\mathbf{e}} \quad (4)$$

3.2. Representative Bird Geometry/Material

Since the irregular shape of a bird poses difficulties in impact problems, a cylinder composed of gelatin with hemispherical ends is selected for its representation [17-20]. The aspect ratio of 2, defined as the length (0.238m) of the cylinder to its diameter (0.119m), is adopted to provide a realistic impact pressure profile [23, 24]. The density of gelatin is 911 kg/m^3, resulting in a bird mass of 2.0 kg approximately. The properties of gelatin used in the simulations are as follows: c_0 = 1.4829×10^3 m/s, s = 2.0367, Γ_0 = 0, η_v = 4×10^{-3} Ns/m^2 [20].

4. Damage and Failure Modes

Materials with reversible behavior are described by generalized Hooke's law. Hashin damage initiation criteria and energy-based damage evolution law are utilized to track various damage modes and mechanisms of composite materials while von Mises yield criteria is selected for isotropic materials.

4.1. Progressive Damage in Fiber-Reinforced Composites

Hashin damage initiation criteria for the composites identify four different damage modes: fiber tension, fiber compression, matrix tension, and matrix compression, as presented in Equations (5) – (8). Damage initiation is detected when the initiation criteria reaches the value of 1.

If $\hat{\sigma}_{11} \geq 0$, fiber tension mode:

$$\left(\hat{\sigma}_{11}/X_T\right)^2 + \alpha_c\left(\hat{\tau}_{12}/S_L\right)^2 \geq 1 \quad (5)$$

If $\hat{\sigma}_{11} < 0$, fiber compression mode:

$$\left(\hat{\sigma}_{11}/X_C\right)^2 \geq 1 \quad (6)$$

If $\hat{\sigma}_{22} \geq 0$, matrix tension mode:

$$\left(\hat{\sigma}_{22}/Y_T\right)^2 + \left(\hat{\tau}_{12}/S_L\right)^2 \geq 1 \quad (7)$$

If $\hat{\sigma}_{22} < 0$, matrix compression mode:

$$\left(\hat{\sigma}_{22}/2S_T\right)^2 + \left[\left(Y_C/2S_T\right)^2 - 1\right]\left(\hat{\sigma}_{22}/Y_C\right) + \left(\hat{\tau}_{12}/S_L\right)^2 \geq 1 \quad (8)$$

The fiber tension mode can be specified by using either the proposed model by setting α_c = 0 and $S_T = Y_C/2$ or the model with α_c = 1 [25, 26].

For the post-damage initiation behavior, the energy dissipation due to failure is taken as the metric and calculated as expressed in Equation (9). The characteristic length of an element is simply computed as the square root of the area associated with the element [27].

$$G^C = \varepsilon_{eq}^f \sigma_{eq}^0 L^c / 2 \quad (9)$$

The effective stress tensor is obtained from the nominal stress tensor and damage operator tensor which embodies three internal damage variables to portray fiber, matrix, and shear damage. Thus it is used to monitor the stiffness degradation of the composite layer enabling progressive damage tracking.

4.2. Shear Failure in Isotropic Materials

The shear failure is described with a simple failure criterion that is suitable for dynamic problems and is based on von Mises stress and equivalent plastic strain, as presented in Equations (10) and (11), respectively [22]. Material yielding starts when von Mises stress reaches the allowable strength of isotropic materials. Then, it is assumed that failure occurs when the equivalent plastic strain corresponds to the failure strain of isotropic materials.

$$\sigma_y = \sqrt{\hat{\sigma}_{11}{}^2 + \hat{\sigma}_{22}{}^2 - \hat{\sigma}_{11}\hat{\sigma}_{22} + 3\hat{\tau}_{12}{}^2} \tag{10}$$

$$\bar{\varepsilon}^{pl} = \bar{\varepsilon}_0^{pl} + \int_0^t \sqrt{(2/3)\dot{\varepsilon}^{pl} : \dot{\varepsilon}^{pl}} \tag{11}$$

4.3. Material Properties and Allowables

The materials used in the blade are balsa wood, UD-GF, GF fabric, and CF fabric. The balsa wood which follows an elastic-perfectly plastic behavior in the simulations has the Young's modulus of 4.1 GPa, Poisson's ratio of 0.3, yield strength of 5.4 MPa, failure strain of 0.8, and density of 155 kg/m^3 [12, 28].

Table 2. Linear Elastic Properties of Composite Materials

	UD-GF	GF fabric $[0/90]_s$	CF fabric $[0/90]_s$
ρ_m (kg/m^3)	2,100	2,100	1,600
E_1 (GPa)	46	21	47
E_2 (GPa)	13	21	47
E_3 (GPa)	13	8.55	10
G_{12} (GPa)	5	3.7	3.78
G_{13} (GPa)	5	3.5	3.5
G_{23} (GPa)	4.6	3.5	3.5
ν_{12}	0.3	0.183	0.33
ν_{13}	0.3	0.0305	0.33
ν_{23}	0.42	0.075	0.07

The homogenized elastic properties of the composite materials are presented in Table 2, and their allowable strength and ultimate strain used to calculate energy dissipation of the composites are presented in Table 3 [29-31]. From Equation (9), the energy dissipation is obtained as a factor of the characteristic length and is presented in Table 3. While von Mises yield criterion is utilized for the balsa wood, Hashin damage model is utilized for the composite materials.

Table 3. Allowable Strength, Strain, and Energy Ratio

	UD-GF	GF fabric $[0/90]_s$	CF fabric $[0/90]_s$
X_T/X_C (MPa)	1,080/620	367/549	627/572
Y_T/Y_C (MPa)	39/128	367/549	627/572
S_L/S_T (MPa)	89/64	97.1/274.5	80/286
$\varepsilon_{1t}^f / \varepsilon_{1c}^f$ (%)	2.8/0.5	2.5/2.5	1.5/1.5
$\varepsilon_{2t}^f / \varepsilon_{2c}^f$ (%)	2.8/0.5	2.5/2.5	1.5/1.5
G_{ft}^C / G_{fc}^C ($\times 10^6$ N/m)	$(15.1/1.55)\times L^c$	$(4.59/6.86)\times L^c$	$(4.70/4.29)\times L^c$
G_{mt}^C / G_{mc}^C ($\times 10^6$ N/m)	$(0.546/0.320)\times L^c$	$(4.59/6.86)\times L^c$	$(4.70/4.29)\times L^c$

5. Element and Mesh Selection

The blade is represented with Lagrangian shell elements that follow the mid-plane shell formulation to avoid the influence of their torsional response [32]. The SW45 blade model with Lagrangian elements is created in HyperMesh, and the mesh size of 0.15 m is employed, generating 41,368 elements. The blade being subjected to aerodynamic loads is analyzed in Abaqus/Standard.

The bird impact problems are analyzed in Abaqus/Explicit. The mesh sizes of 0.02 m and 0.01 m are employed for Lagrangian and Eulerian elements, respectively, determined based on the study for the optimal ratio of Lagrangian to Eulerian elements [4]. The TSB5M blade is modeled with Lagrangian elements and contains 64,500 elements while 1,200,000 Eulerian elements are used to define the domain that contains the bird.

5.1. Lagrangian Description

3D linear conventional shell elements are appropriate since the blade thickness is significantly smaller than any other global in-plane dimensions such as the blade tip radius or chord length. Accordingly, the blade is represented with S3R/S4R shell elements, which are suitable for nonlinear geometrical analyses. S3R and S4R are a 3-node, trilateral, and 4-node, quadrilateral, stress/displacement, shell element, respectively. These elements have three displacement and three rotational degrees of freedom (DOF) and allow finite strain, arbitrarily large rotations, and transverse shear deformation [22].

5.2. Eulerian Description

Eulerian elements represent stationary rectangular grids and allow a material to flow through the elements and to interact with Lagrangian element structure. Eulerian elements overcome numerical difficulties associated with excessive element distortion. The element geometry is not conformed to the boundary of Eulerian materials at any time during analysis. Thus, materials are assigned to Eulerian

elements by means of volume fraction. 3D Eulerian elements (EC3D8R) in Abaqus/Explicit are adopted in the models. EC3D8R is an 8-node linear brick which accommodates multi-material definition and reduced integration with hourglass control. Note that the nodes of Eulerian elements are independent from Lagrangian S3R/S4R shell elements [22].

6. Loading Conditions

6.1. Lift and Drag Forces

Aerodynamic loads such as lift and drag forces are dependent on wind speed. For large-scale HAWTs, their maximum values usually occur at nominal wind speed (10-12 m/s). Lift and drag forces of an infinitesimal blade element are calculated using two-dimensional airfoil characteristics, disregarding the velocity along the rotor radius and three-dimensional effects. When the X-axis of the blade is aligned with the x-axis of the wind turbine (Figure 1), lift and drag forces for the rotating blade with an angle of attack are generated. The contribution of lift forces along the y-axis enables the blade to rotate while the decomposed component of drag forces along the y-axis acts on the blade to resist its rotation. Resultant relative wind velocity for the rotating blade is represented by Equation (12) [33]. Note that the wind speed is aligned to the z-axis of the wind turbine.

$$V_{rel} = \sqrt{{u_w}^2 + {u_{ta}}^2} \tag{12}$$

Lift forces normal to a resultant relative wind velocity and drag forces parallel to a resultant relative wind velocity are expressed in Equation (13) [33].

$$\delta L/c\delta r = \rho_{air} {V_{rel}}^2 C_l /2 \;\; \& \;\; \delta D/c\delta r = \rho_{air} {V_{rel}}^2 C_d /2 \tag{13}$$

Air density is selected to reflect the tower height. Lift and drag coefficient corresponding to the limit angle of attack is selected to have the upper limit of C_l in a low-drag lift coefficient range [8]. The tangential velocity of the blade is linear speed of the rotating blade with a constant angular velocity (Ω) which varies along the rotor radius. The ratio of tangential velocity of the blade to wind speed at r is presented in Equation (14). At the blade tip (i.e., $r = R$), Equation (14) can be rewritten in Equation (15), called a TSR [33, 34].

$$\lambda = u_{tb}/u_w = r\Omega/u_w \tag{14}$$

$$\mathrm{TSR} = R\Omega/u_w \tag{15}$$

Herein, the TSR is assumed to be a constant value, and the speed ratio linearly increases along the rotor radius. For a given wind speed and TSR value, angular velocity of the blade can be determined from Equation (15). The tangential velocity of the blade along the rotor radius can be obtained from Equation (14). Finally, the resultant of each decomposed load component along the blade Y- and Z-axis become, respectively:

$$dP_Z = \left(\delta L/c\delta r\right)\cos\alpha_l + \left(\delta D/c\delta r\right)\sin\alpha_l \tag{16a}$$

and

$$dP_Y = -\left(\delta L/c\delta r\right)\sin\alpha_l + \left(\delta D/c\delta r\right)\cos\alpha_l \tag{16b}$$

The three rotations and three displacements are constrained at the blade root; the Z component of the resultant forces is applied to the lower shell surface of the blade; the Y component of the resultant forces is applied both to the lower and upper shell surfaces, as shown in Figure 4.

Air density is assigned as 1.208 kg/m^3 for 140 m tower (hub) height. The TSR of the blade is assumed to be constant at 7 [34]. The maximum lift and drag forces associated with u_w = 12 m/s are considered. Since tangential velocity of the blade is not constant along the rotor radius, lift and drag forces are evaluated along eight sections [4, 5].

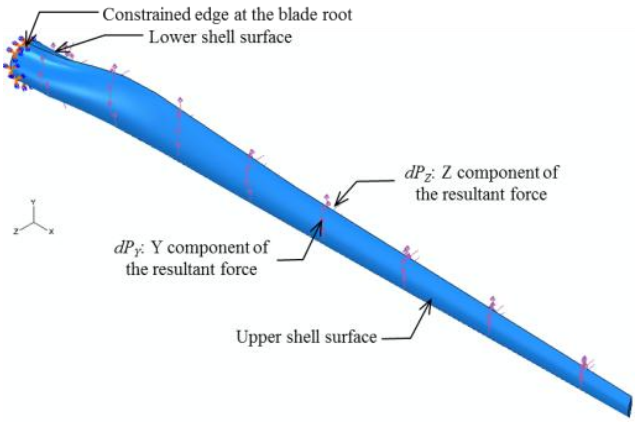

Figure 4. Boundary conditions for static analyses in the blade

6.2. Bird Impact

The CEL approach is employed to simulate the blade-bird strike in Abaqus/Explicit. The Lagrangian target structure for a bird impactor is the 5m tip section of the 80m blade while the 2kg gelation bird is considered as a soft body and modeled with Eulerian elements (EC3D8R). Due to the fixed Eulerian mesh, the boundary of the bird is recomputed in each time increment as it flows through the mesh. Accordingly, gelatin is assigned to Eulerian elements by means of Eulerian volume fraction (EVF) that represents the ratio by which each Eulerian element is filled. Volume fraction of 0 indicates that the elements are not filled at all (i.e., they constitute a void); on the contrary the volume fraction of 1 states that the elements are completely filled with gelatin as seen in Figure 5 [22]. Thus, the bird is represented inside the Eulerian domain with a combination of fully and partially filled elements surrounded by void regions. Direct and oblique impact scenarios are considered, and the impact location is at r = 77.5 m. No initial displacements and stresses are applied to the target structure. A general contact algorithm, which automatically detects which surfaces and edges come into contact, with a penalty method and frictionless surface is employed in the simulations [19, 35].

For the direct and oblique impact scenarios, the edges of the blade at r = 75 m are fully constrained, and a time period of 0.01s is considered. For the event of the direct impact, the 2kg bird is assumed to have a translational velocity of 81.4 m/s, and the impact point is the leading edge. This initial velocity is prescribed along the blade Y-axis in the Eulerian domain and is representative of the rated velocity of the rotating blade at the impact point.

For the oblique impact, the bird is initially located at r = 77.5 m at an impact angle of 30 °to the lower forward blade skin as seen in Figure 5. The initial velocity along the blade Y- and Z-axis is assigned as 70.5 m/s and 40.7 m/s, respectively, leading to 81.4 m/s of resultant velocity.

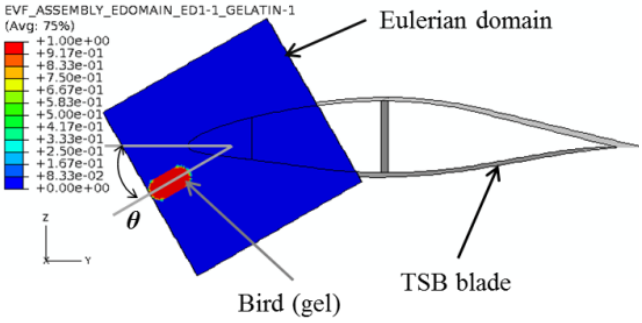

Figure 5. The bird described by EVF on the cross-sectional view at r = 77.5 m for the direct impact (θ = 0 °) and oblique impact (θ = 30 °)

7. Results and Discussion

Herein we present results for the 80 m blade (SW45) which is subjected to lift and drag force and for the 5 m tip sectional blade (TSB5M) subjected to direct as well as oblique impact.

7.1. Deformation

7.1.1. Tip Displacements due to Aerodynamic Load

The tip displacements for SW45 are presented at the loads corresponding to wind velocity of u_w = 8.72 m/s where the von Mises stress of the balsa core reaches its allowable strength. Thus, it is regarded as core damage.

At the onset of the core damage, the U_3 tip displacements are much larger than the other displacement components. The blade undergoes U_3 tip displacement of 4.96 m, corresponding to 6.2% of the blade tip radius.

7.1.2. Direct Impact: Deformed Shape

The U_2 displacement of the blade at 0.0025s and 0.01s during direct impact is presented in Figure 6 where the maximum values at the impact site are 6.61×10^{-4} m and 2.50×10^{-4} m, respectively. These displacements are rather small and remain localized at the impact site. As the impact forces are released, the blade starts fluctuating locally and elastic deformation recovery causes the decrease in U_2 displacements from 0.0025s to 0.01s.

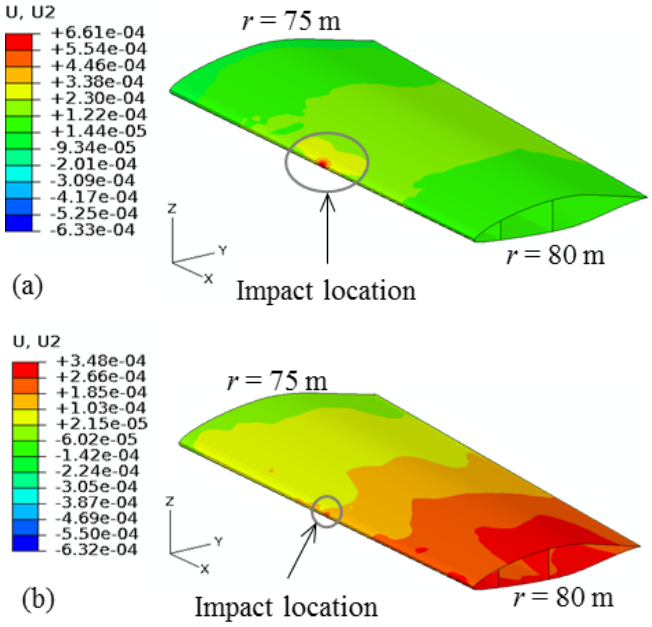

Figure 6. Global U_2 displacement of the 5m tip sectional blade: (a) 0.0025s, and (b) 0.01s

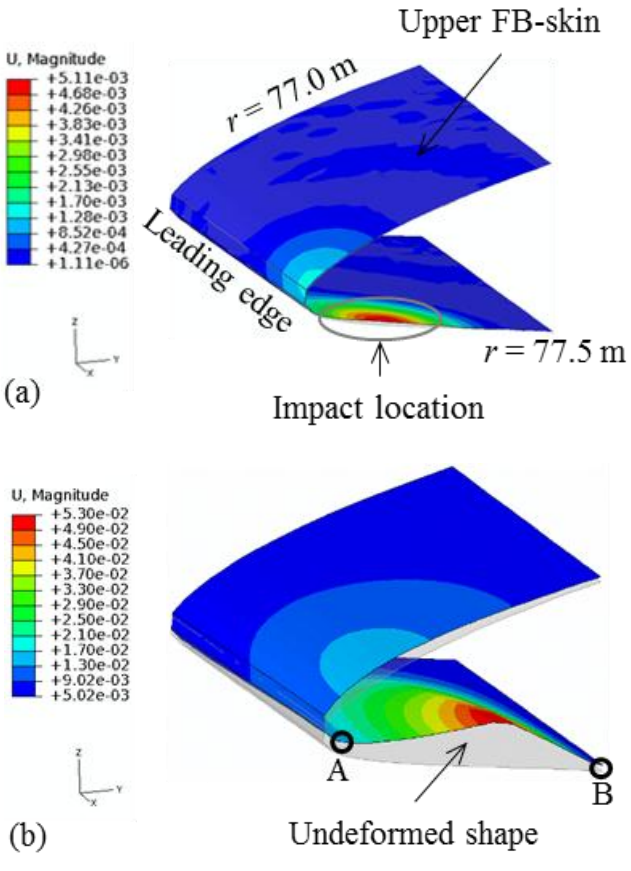

Figure 7. The magnitude of the displacements of the FBS (77 m < r < 77.5 m) in TSB5M: (a) 0.002s, and (b) 0.006s

7.1.3. Oblique Impact: Deformed Shape

As shown in Figure 7(a), the event of the oblique impact

starts at 0.002s when the lower forward blade skin (FBS) locally deflects inward. The deformed shape of the lower FBS on the cutaway view at r = 77.5 m is changed from an arc to a triangle. As shown in Figure 7, the maximum magnitude of the displacements is 0.053 m at 0.006s. The oblique impact does not cause any contact between the upper and lower FBSs. Since the lower FBS toward the skin/spar cap (Point B) is adjacent to the stiff spar cap and shear web, the displacement at Point B is lower than at Point A. After 0.006s, local fluctuation and elastic deformation recovery lead to a decrease in the magnitude of the displacements.

7.2. Motional State of the Bird during Direct Impact

The EVF contour of the Eulerian domain in the case of the direct impact is presented in Figure 8 to describe the motion of the bird (gel flow). Note that the unfilled elements (i.e., the EVF value of zero) are deleted in the Eulerian domain of Figure 8 for better visualization. First, the gel contacts the leading edge of the blade and starts flowing in two directions (i.e., over the upper and lower blade skin) forming a parabola with increasing time. The contact area between the blade and the gel is rather small around the leading edge, and the gel is split by the sharp form of the airfoil. This configuration helps to reduce the impact forces and thus diminishes the blade deformation.

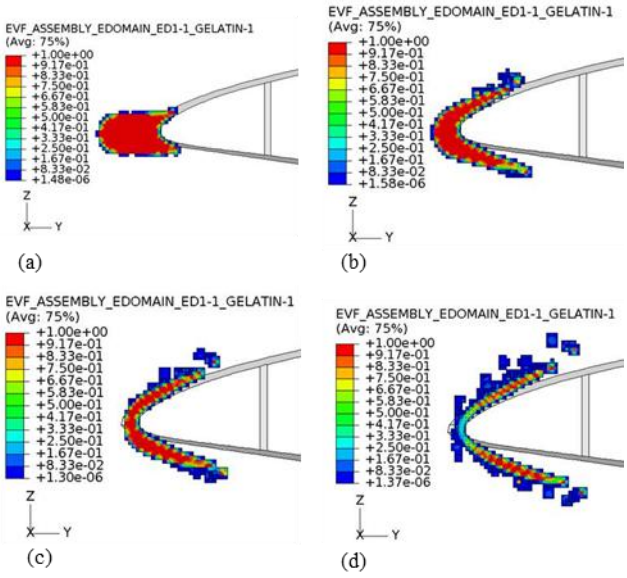

Figure 8. Motional states of the gel's EVF on the cross-sectional view at r = 77.5 m: (a) 0.001s, (b) 0.0025s, (c) 0.003s, and (d) 0.004s

7.3. Stress Fields and Damage Mechanisms in SW45 Blade

The distance of the outer layer from the centroid of the blade cross-section is greater than that of the inner layer. Also, thickness of the layers is much smaller compared to the distance from the centroid creating higher section modulus in the outer layer than the inner layer. Thus, higher stresses appear in the outermost layer.

S_{11} stresses in the outermost GF fabric layer of the upper blade skin (46 m < r < 80 m) for SW45 blade at u_w = 12 m/s are presented in Figure 9. The highest compressive stress magnitude of 94.5 MPa occurs in the skin/spar cap around r = 70 m as seen in Figure 9. However, this value is significantly less than the allowable strength (X_C =549 MPa). Flipping in the sign of S_{11} stress in the skin/spar cap located at 60 m < r < 75 m as seen in Figure 9 indicates presence of warping. Thus, the tensile stresses are seen inside the warp, and the compressive stresses are experienced in the skin/spar cap region outside the warp. This is attributed to the absence of balsa core, as well as insufficient reinforcement by the spar cap in this configuration.

Overall the stresses in the GF and CF layers are very small in comparison to their respective allowable strength values. The maximum value of Hashin damage initiation criteria in all composite layers at u_w = 12 m/s is below the damage initiated state value of 1. Therefore, no damage in the GF and CF layers in the root, skin, spar cap, and shear web are experienced in SW45 blade.

The balsa core of the aft blade skin defined as 60 m < r < 70 m experiences the highest compressive S_{11} stress of 5.99 MPa as illustrated in Figure 10. In such high stress locations, it is concluded that balsa wood core is not the best option.

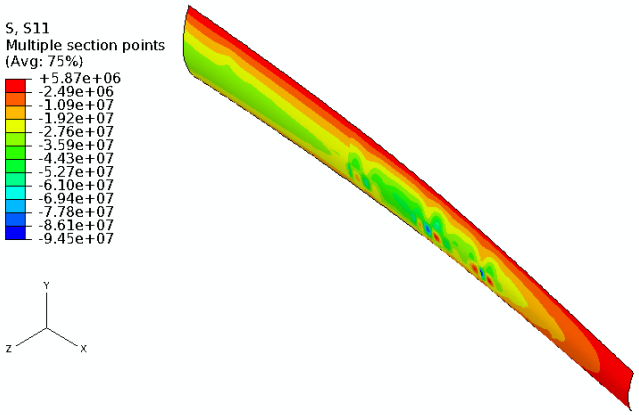

Figure 9. S_{11} stress contour in the outermost GF fabric layer of the upper blade skin (46 m < r < 80 m) for SW45 at u_w =12 m/s

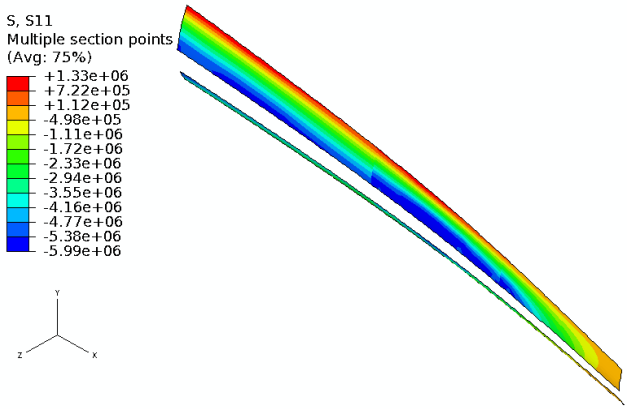

Figure 10. S_{11} stress contour in the balsa core of the upper blade skin (46 m < r < 80 m) for SW45 at u_w =12 m/s

7.3.1. Core Damage

Although balsa cores are used to prevent local buckling mode, yielding of the core starts at u_w = 8.72 m/s. The von Mises stresses in the core of the skin and web at u_w = 12 m/s are presented in Figure 11.

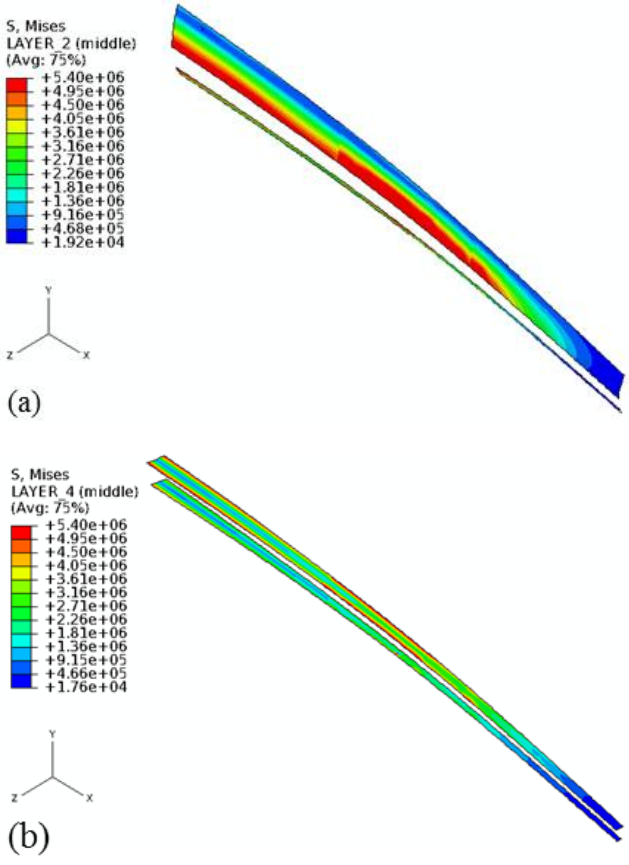

Figure 11. Von Mises stress contour in the balsa core for SW45 at u_w =12 m/s: (a) the upper blade skin (46 m < r < 80 m), and (b) the web (46 m < r < 80 m)

The highest von Mises stresses spread from the boundary between the skin/spar cap, and the skin and/or web. The yielding of the balsa is seen in the forward skin (20 m < r < 32 m and 60 m < r < 70 m), aft skin (20 m < r < 32 m and 46 m < r < 75 m), forward web (20 m < r < 32 m), and aft web (20 m < r < 32 m and 46 m < r < 70 m) at u_w =12 m/s. The elemental areas where yielding takes place are normalized with respect to the surface area of the skin or web in that region. For example, the upper and lower aft skin experience 22.7%-33% in the region defined as 60 m < r < 70 m. Furthermore, the changes in the airfoil thickness also contribute to this failure mode.

7.3.2. Damage due to Direct Impact

The structural components of the hybrid blade (sandwich skin, shear web, and spar cap) of the 5m blade are much more rigid than the soft body of the bird. Even though overall small deformations are observed at the time of impact, von Mises stress in the balsa core of the forward blade skin reaches its allowable strength of 5.4 MPa at the impact site. Thus, yielding of the balsa occurs at 0.0005s, generating an equivalent plastic strain of 0.01 at 0.006s as shown in Figure 12. Afterward, the plastic strain does not increase since the impact energy has already been dissipated at the leading edge. Throughout the event, the balsa core in the shear web remains below its allowance. Furthermore, no damage initiation and progression caused by the direct impact are observed in any of the composite layers.

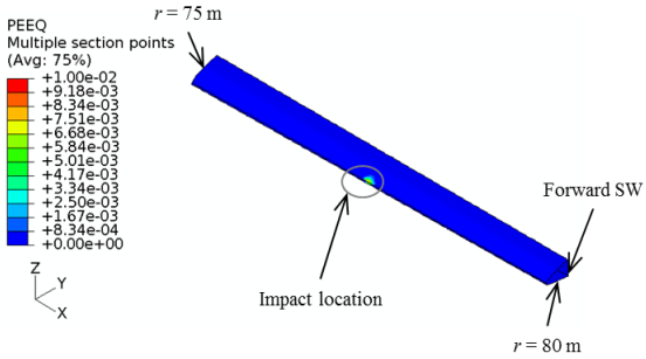

Figure 12. Equivalent plastic strain in the balsa of the FBS and SW at 0.006s

7.3.3. Damage due to Oblique Impact

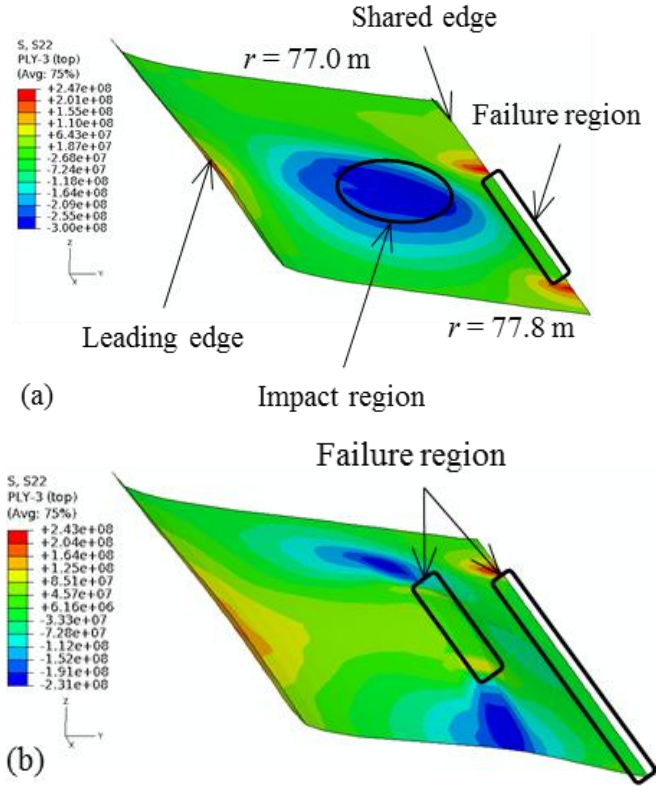

Figure 13. S_{22} stress in the outermost GF fabric of the lower FBS (77 m < r < 77.8 m): (a) 0.004s, and (b) 0.006s

In the event of the oblique impact, the bird, initially located at r = 77.5 m, contacts the lower FBS. The lower FBS bulges out in the positive Z-axis, creating the highest

compressive S_{22} stress (300 MPa) at 0.004s as shown in Figure 13. The highest tensile stress is 247 MPa near the shared edge at 0.004s. Matrix tensile damage is observed over a region that is 0.42 m in length with a surface area of 7.9×10^{-3} m^2 as depicted in Figure 13(a). Note that the tensile stress that occurs at the center of the impact region at 0.005s causes matrix tension damage at 0.006s as seen in Figure 13(b). Consequently, the fabric layer located in this failure region is much weaker and softer than UD-GF layer and susceptible to extremely high strains in the 2-direction.

At 0.004s, the highest tensile S_{22} stress (346 MPa) is generated in the higher stress region as displayed in Figure 14(a). Simultaneously, the highest compressive S_{22} stress (210 MPa) occurs in the vicinity of the shared edge. Only a single element with its area of 3.6×10^{-4} m^2 in the high stress region of Figure 14(a) reaches the Hashin initiation criteria of 1. Note that the value for S_{22} stress in the failure region of Figure 14(b) is zero at 0.0045s since the fabric layer is degraded to reflect its matrix tensile damage mode. This region is described as 0.37 m long by 1.9×10^{-2} m wide at 0.0045s. Despite its growth to 0.64 m in length at 0.006s, it did not experience any additional damage modes. Comparing contours of Figures. 13 and 14, leads to the conclusion that the failure region near the shared edge occurs in the outermost layer only. As noted, the innermost layer at the impact site is damaged earlier and deformed severely after 0.0045s causing the increase in the S_{22} tensile stress in the outermost layer.

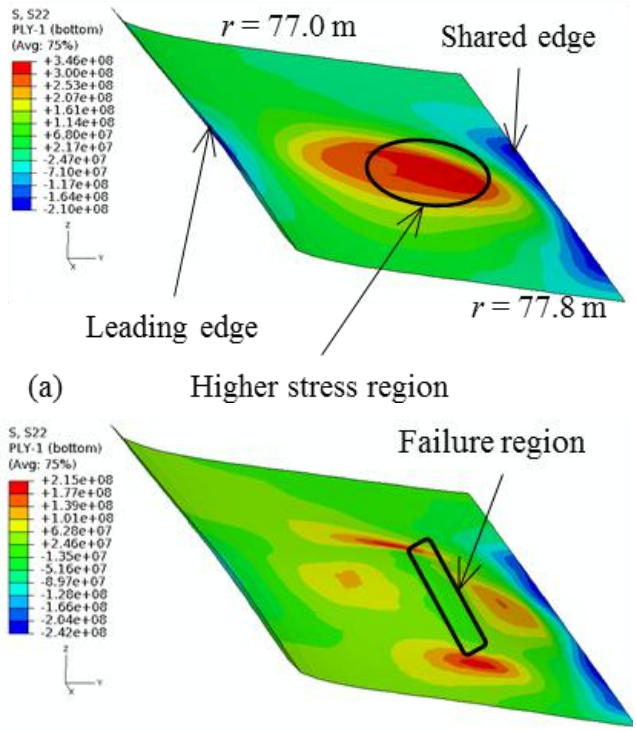

Figure 14. S_{22} stress in the innermost GF fabric of the lower FBS (77 m < r < 77.8 m): (a) 0.004s, and (b) 0.0045s

The von Mises stress in the core of the lower FBS is presented in Figure 15. It is reported at the mid-plane of the shell elements corresponding to the neutral plane of the balsa. After the bird strikes against the lower FBS, the von Mises stress in the core within the vicinity of the leading edge reaches its allowable strength at 0.002s, as seen in Figure 15(a). Yielding occurs at 5.4 MPa at this location where the congruence of geometric complexities of large curvature and leading edge contribute to stress concentrations. As the deformation is larger in the impact region, the yielding region is expanded along the Y-axis as seen in Figure 15(b) at 0.005s.

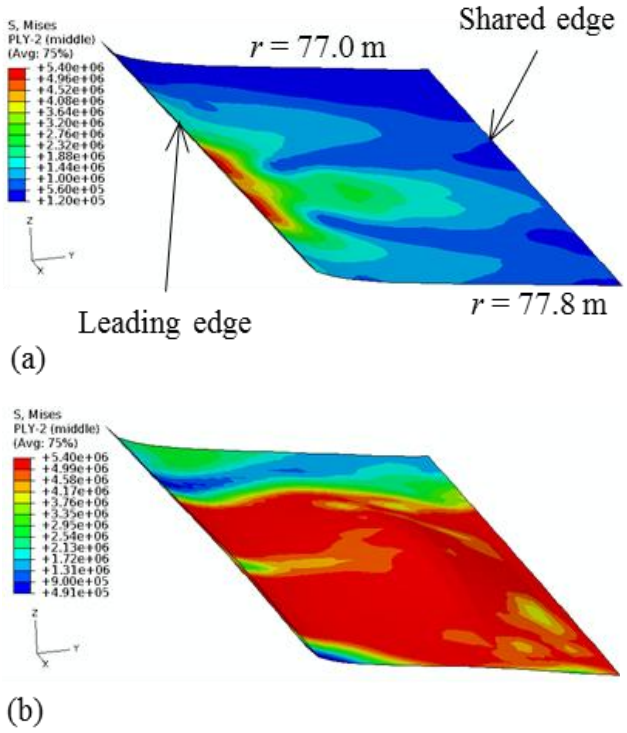

Figure 15. Von Mises stress in the balsa of the lower FBS (77 m < r < 77.8 m): (a) 0.002s, and (b) 0.005s

8. Conclusions

In the 80 m full-length blade model, the largest displacements occurred along the blade Z-axis where the resultant aerodynamic forces were the largest. The largest U_3 tip displacement was 6.2% of the blade tip radius when yielding in the balsa core ensued under the loads associated with wind speed, u_w = 8.72 m/s. Since Hashin damage initiation criteria in all composite layers were below the damage state value of 1, the GF and CF layers of the blade root, skin, shear web, and spar cap were not damaged. The S_{11} stress in the GF fabric face of the sandwich skin was several times higher than that in the balsa core since the core was stiffer and weaker compared with the GF face materials. Furthermore, flipping the sign of S_{11} stress in the upper skin/spar cap (60 m < r < 75 m) indicated the formation of a warp which potentially could lead to wrinkling. Thus, the blade configuration provided sufficient damage tolerance below the loads associated with u_w = 8.72 m/s.

The 2kg bird upon the direct impact with the 5m tip section of the 80m blade caused a small U_2 displacement (up

to 6.61×10^{-4} m). This impact scenario created minor and localized deformation in the blade since the contact area between the blade and bird remained small due to the sharp airfoil shape at the leading edge to reduce the transfer of impact forces to the blade effectively. However, the balsa core in the forward blade skin exceeded its yield strength. Stresses in composite layers were much smaller than their allowable strength. Thus, no damage initiation in the composite layers was found during direct impact.

In the oblique impact scenario, the balsa core exceeded its yield near the leading edge at 0.002s. Matrix tensile damage initiation and progression in the GF fabric layer was observed at the following locations: at outermost layer at the shared edge with shear web and skin/spar at 0.004s, at the innermost layer at the impact location at 0.0045s, and at the outermost layer at the impact location at 0.006s. However, the bird did not penetrate the lower forward blade skin. While the direct impact configuration effectively reduced the transfer of impact forces to the blade, the oblique impact forces were dissipated on the impact site where tensile damage/failure mode was observed.

Nomenclature

C_l = lift coefficient
C_d = drag coefficient
c = chord
c_0 = bulk speed of sound
dP_Y = Y component of the resultant forces
dP_Z = Z component of the resultant forces
d_f = fiber damage variable
d_m = matrix damage variable
d_s = shear damage variable
E_m = specific energy
$\dot{\mathbf{e}}$ = deviatoric part of a strain rate tensor
L = length of an impactor
p = pressure
R = blade tip radius
r = local rotor radius of a blade
$\mathbf{S}$ = deviatoric stress tensor
S_L = longitudinal shear strength
S_T = transverse shear strength
s = material constant of a bird model
t = blade thickness
t_d = total duration of an impact event
TSR = tip speed ratio
U_p = particle velocity
U_s = shock velocity
u_w = wind speed
V_{rel} = resultant relative wind velocity for the rotating blade
u_{ta} = tangential air flow velocity
u_{tb} = tangential velocity of the blade
X_C = longitudinal compressive strength
X_T = longitudinal tensile strength
Y_C = transverse compressive strength
Y_T = transverse tensile strength
α = angle of attack
α_c = coefficient to determine the contribution of the shear stress to the fiber tension mode
α_l = limit angle of attack
Γ_0 = material constant of a bird model
$\delta\mathbf{D}$ = drag force for the rotating blade
$\delta\mathbf{L}$ = lift force for the rotating blade
δr = infinitesimal blade length
$\dot{\varepsilon}^{pl}$ = equivalent plastic strain rate
ε_{eq}^{f} = equivalent strain where the material is considered failure completely
$\bar{\varepsilon}_0^{pl}$ = initial value of the equivalent plastic strain
η = nominal volumetric compressive strain ($=1-\rho_0/\rho$)
η_v = viscosity of a bird model
λ = tangential velocity of the blade to wind speed at r
ρ = current density of a bird model
ρ_0 = reference density of a bird model
ρ_{air} = air density
ρ_{gel} = density of gelatin
$\hat{\sigma}_{ij}$ = components of the in-plane effective stress tensor
σ_y = von Mises stress
σ_{eq}^{0} = initial equivalent stress where the initiation criteria are met

REFERENCES

[1] U.S. Energy Information Administration. (2016) International energy outlook 2016. [Online]. Available: http://www.eia.gov/forecasts/ieo/pdf/0484(2016).pdf.

[2] Archer, C.L., Jacobson, M.Z., 2005, Evaluation of global wind power, J. Geophys. Res. Atmos., 110 (D12), D12110.

[3] Energy Efficiency and Renewable, "20% wind energy by 2030: increasing wind energy's contribution to U.S. electricity supply," U.S. Department of Energy, Washington, DC, DOE/GO-102008-2567, 2008.

[4] N. Nanami, "Structural and damage assessment of multi-section modular hybrid composite wind turbine blade," Ph.D dissertation, Texas A&M University, College Station, TX, 2014.

[5] N. Nanami, O.O. Ochoa, Vibration and Dynamic Response of Hybrid Wind Turbine Blades. D. Liu, Ed. Dynamic Effects in Composites Materials, Vol. 1, Lancaster, PA: DEStech Publications, 2012.

[6] Nanami, N., Ochoa, O.O., 2013, Bird impact study of a preloaded composite wind turbine blade, Proc. 19th International Conf. on Composite Materials, Montreal, Canada, 6415.

[7] D.S. Berry, D. Berg, "Blade system design studies phase II: final project report," Sandia National Laboratories, Albuquerque, NM, SAND2008-4648, 2008.

[8] D. Somers, "The S816, S817, and S818 airfoils," National Renewable Energy Laboratory, Golden, Co, NREL /SR-500-36333, 2004.

[9] Timmer, W.A., van Rooij, R., 2003, Summary of the Delft university wind turbine dedicated airfoils, J. Sol. Energ., 125 (4), 488-496.

[10] Fuglsang, P., Bak, C., 2004, Development of the Risø wind turbine airfoils, Wind Energy, 7 (2), 145-162.

[11] Thomsen, O.T., 2009, Sandwich materials for wind turbine blades - present and future, J. Sandw. Struct. Mater., 11 (1), 7-26.

[12] Todoroki, A., Kawakami, Y., 2008, Optimal design of wind turbine blade of CF/GF hybrid composites, Trans. JSCES, 2008 (2008), 20080012 [in Japanese].

[13] D.A. Griffin, "Blade system design studies volume I: composite technologies for large wind turbine blades," Sandia National Laboratories, Albuquerque, NM, SAND2002-1879, 2002.

[14] D.A. Griffin, "Blade system design studies volume II: preliminary blade designs and recommended test matrix," Sandia National Laboratories, Albuquerque, NM, SAND2004-0073, 2004.

[15] Dahlroth, D., 1983, Load cases for medium-sized wind power plants, Proc. Structural Design Criteria for LS WECS, Greenford, UK, 121-193.

[16] Castelletti, L.M.L., Anghileri, M., 2003, Multiple birdstrike analysis - a survey of feasible techniques, Proc. the 30th European Rotorcraft Forum, Marseilles, France, 495-505.

[17] Heimbs, S., 2011, Computational methods for bird strike simulations: a review, Comput. Struct., 89 (23-24), 2093-2112.

[18] Heimbs, S., 2011, Bird strike simulations on composite aircraft structures, Proc. 2011 SIMULIA Customer Conf., Barcelona, Spain, 73-86.

[19] Shmotin, Y., Chupin, P., Gabov, D., Ryabov, A., Romanov, V., Kukanov, S., et al., 2009, Bird strike analysis of aircraft engine fan, Proc. the 7th European LS-DYNA Conf., Salzburg, Austria, H-I-03.

[20] McCallum, S., Constantinou, C., 2005, The influence of bird-shape in bird-strike analysis, Proc. the 5th European LS-DYNA Users Conf., Birmingham, UK, 2c-77.

[21] C. B. Hasager, A. Peña, T. Mikkelsen, M.S. Courtney, I. Antoniou, S.E. Gryning, et al., "12MW horns rev experiment," Risø National Laboratory, Roskilde, Denmark, Riso-R-1506(EN), 2007.

[22] ABAQUS, Inc, ABAQUS Documentation Collection, Ver. 6.12, Pawtucket, RI: ABAQUS, Inc., 2012.

[23] Airoldi, A., Cacchione, B., 2006, Modelling of impact forces and pressures in Lagrangian bird strike analyses, Int. J. Impact Eng., 32 (10), 1651-1677.

[24] Johnson, A.F., Holzapfel, M., 2003, Modelling soft body impact on composite structures, Compos. Struct., 61 (1-2), 103-113.

[25] Hashin, Z., Rotem, A., 1973, A fatigue failure criterion for fiber reinforced materials, J. Compos. Mater., 7 (4), 448-464.

[26] Hashin, Z., 1980, Failure criteria for unidirectional fiber composites, J. Appl. Mech., 47 (2), 329-334.

[27] Lapczyk, I., Hurtado, J.A., 2007, Progressive damage modeling in fiber-reinforced materials, Compos. Part A, 38 (11), 2333-2341.

[28] Vural, M., Ravichandran, G., 2003, Microstructural aspects and modeling of failure in naturally occurring porous composites, Mech. Mater., 35 (3-6), 523-536.

[29] M.D. Daniel, O. Ishai, Engineering Mechanics of Composite Materials, New York, NY: Oxford University Press, 1994.

[30] Kyriazoglou, C., Guild, F.J., 2006, Finite element prediction of damping of composite GFRP and CFRP laminates: a hybrid formulation–vibration damping experiments and Rayleigh damping, Compos. Sci. Technol., 66 (3-4), 487-498.

[31] MatWeb. (2010) Greene tweed orthetek WF polyketone, continuous woven carbon fiber, Database of material properties. [Online]. Available: http://www.matweb.com/search/QuickText.aspx?SearchText=woven%20carbon.

[32] Laird, D.L., Montoya, F.C., Malcolm, D.J., 2005, Finite element modeling of wind turbine blades, Proc. AIAA/ASME Wind Energy Symposium, Reno, NV, 9-15.

[33] T. Burton, N. Jenkins, D. Sharpe, E. Bossanyi, Wind Energy Handbook, New York, NY: Wiley, 2011.

[34] E. Hau, Wind Turbines: Fundamentals, Technologies, Application, Economics, 2nd ed., New York, NY: Springer-Verlag, 2006.

[35] Benson, D.J., Okazawa, S., 2004, Contact in a multi-material Eulerian finite element formulation, Comput. Methods in Appl. Mech. Eng., 193 (39-41), 4277-4298.